








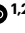
Achieving the full-wavelength phase-matching for efficient nonlinear optical frequency conversion in $\text{C}(\text{NH}_2)_3\text{BF}_4$

Received: 5 December 2022

Accepted: 3 May 2023

Published online: 12 June 2023

 Check for updates

Miriding Mutailipu ^{1,2,4}, Jian Han ^{1,2,4}, Zhi Li ³, Fuming Li ^{1,2}, Junjie Li ^{1,2}, Fangfang Zhang ^{1,2}, Xifa Long^{1,2}, Zhihua Yang ^{1,2} & Shilie Pan ^{1,2} ✉

Phase-matching of light waves is a critical condition for maximizing the efficiency of nonlinear frequency conversion processes in nonlinear optical crystals; however, phase-matching, commonly achieved by tuning birefringence, is often difficult to achieve over a wide wavelength range. Here, full-wavelength phase-matching crystals that can avoid phase-mismatching across the entire optical transparency range are proposed. The anisotropic strength of bonding in the dimension of energy is confirmed theoretically to be the key to the full-wavelength phase-matching ability. We demonstrate that a crystal of guanidinium tetrafluoroborate ($\text{C}(\text{NH}_2)_3\text{BF}_4$) can be phase-matched throughout its entire optical transparency range and is able to generate harmonic light as short as ~ 193.2 nm, which is close to its deep-ultraviolet cut-off edge. Importantly, this crystal is stable, cheap and efficient compared with commercially available nonlinear optical crystals for generation of 266 nm light. This work lays the foundation for finding a new class of crystals in which the phase-matching wavelength fully covers its optical transparency range, and also provides a high-performance crystal for generating light at 266 nm—the fourth-harmonic of a commercial 1,064 nm laser.

Nonlinear optical (NLO) frequency conversion, which enables a deterministic modulation of light's wavelength and polarization, laid the foundations for harmonic generation, optical manipulation and photon entanglement, and so on^{1–5}. Phase-matching is a condition for which the output signal during the frequency conversion process is maximized when considering the conservation of photon momentum. Put simply, for three-wave interactions within a second-harmonic generation (SHG) process, phase-matching occurs when the relation of $k(2\omega) = 2k(\omega)$ or $n(2\omega) = n(\omega)$, making the wave vector difference $\Delta k = 0$, in which k , ω and n represent the wave vector, angular frequency and

refractive index, respectively (refs. 1,2). This represents the best-case scenario for conversion efficiency in a nonlinear process; however, due to material dispersion, the three interacting beams do not propagate in phase, resulting in destructive interference and an extremely low conversion efficiency. This so-called phase-matching problem (or phase-mismatching) became immediately evident when the first attempt to describe such a condition was made for the quadratic nonlinear process in 1962⁶. Compensating for phase-mismatching is therefore an important challenge, and subsequent efforts have focused on developing new technologies and experimental verifications^{7–12}.

¹Research Center for Crystal Materials, Xinjiang Technical Institute of Physics and Chemistry, Chinese Academy of Sciences, Urumqi, People's Republic of China. ²Center of Materials Science and Optoelectronics Engineering, University of Chinese Academy of Sciences, Beijing, People's Republic of China. ³MIIT Key Laboratory of Advanced Display Materials and Devices, Institute of Optoelectronics and Nanomaterials, School of Materials Science and Engineering, Nanjing University of Science and Technology, Nanjing, People's Republic of China. ⁴These authors contributed equally: Miriding Mutailipu, Jian Han. ✉ e-mail: slpan@ms.xjb.ac.cn

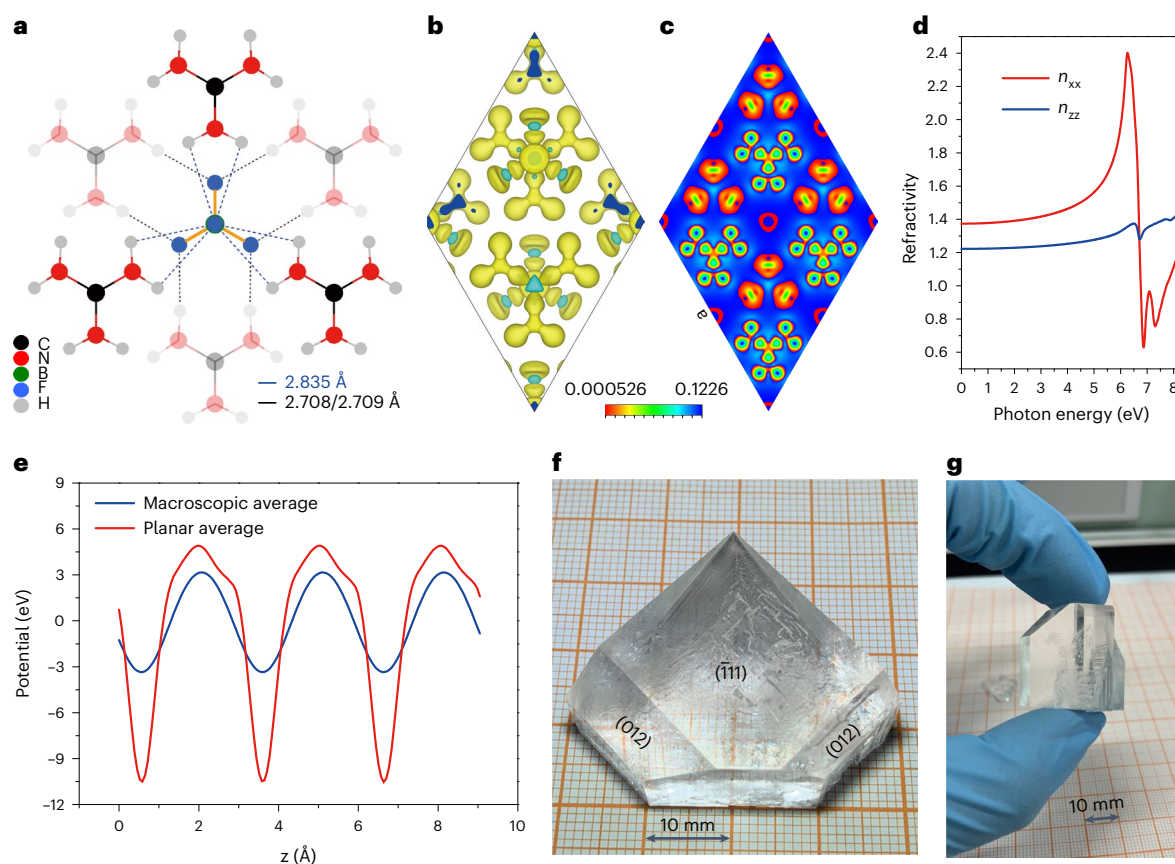


Fig. 1 | Crystal structure, microstructural analysis and as-grown single crystal. **a**, Crystal structural features of GFB with the emphasis on hydrogen bond interactions between the $[C(NH_2)_3]$ and $[BF_4]$ units. More detailed features describing the structures are shown in Supplementary Fig. 1. **b**, **c**. The three-**(b)** and two-dimensional **(c)** charge density difference plots of GFB for the (001) plane. Colour scale information for **b**: isosurface level, 0.0249988; model, positive and negative; colour, yellow RGB 255, 255, 0. The isovalue increases from

red to blue across the region from 0.000526 to 0.1226 in **c**. **d**. Calculated refractive indices versus photon energy using the derived formula. A substantial difference between n_{xx} and n_{zz} is observed, especially in regions close to the band gap of GFB, where n_{xx} increases suddenly and n_{zz} curves remain relatively flat. **e**. The curves of the calculated electrostatic potential in GFB, which is not parabolic due to broken spatial inversion symmetry. **f**, **g**. Photographs of an as-grown GFB crystal. See Methods for details on the growth process and equipment used.

The phase-matching condition of $n(2\omega) = n(\omega)$ is very tough where the incident and second harmonic light have different polarizations, and birefringence is currently widely employed to implement the phase-matching. Birefringent phase-matching matches the phase velocity of interaction waves to overcome dispersion and suppresses phase-mismatching, aided by polarization-dependent indices in a certain spectral region^{1,2,13}. This is, however, limited by the dispersion of naturally occurring crystals, which prevents them from achieving phase-matching throughout the entire optical transparency range when using a direct SHG process. This situation results in a loss between the phase-matching wavelength limit (also known as the shortest phase-matching wavelength, λ_{PM}) and the ultraviolet cut-off edge ($\lambda_{cut-off}$), and thus the transparency range cannot be fully utilized (typically with $\lambda_{PM} > \lambda_{cut-off}$), resulting in phase-mismatching in the region of $[\lambda_{cut-off}, \lambda_{PM}]$. The loss of phase-matching wavelength $\Delta\lambda_L = \lambda_{PM} - \lambda_{cut-off}$ is evident for NLO oxides applied to varying spectral regions under the SHG phase-matching condition¹⁴, and so far this is inevitable for all NLO crystals. Alternatively, the advent of quasi-phase-matching approach can, in principle, achieve nonlinear frequency conversion within the whole optical transparency range^{8,12,15,16}, in which the nonlinear properties are made to vary periodically, typically by reversing the sign of nonlinear coefficients; however, quasi-phase-matching is more complex to implement, requiring the use of multiple laser beams or carefully engineered geometries, which limits its practical application to only

a few NLO crystals, especially in the short-wavelength ultraviolet and deep-ultraviolet regions.

Interestingly, a past review paper raised the question of whether the ideal state (where λ_{PM} is equal to, or almost close to, $\lambda_{cut-off}$) could be achieved in NLO crystals based on birefringent phase-matching¹⁷. To answer this question, in this work we propose a new class of crystals that can phase-match across its whole optical transparency range, termed full-wavelength phase-matching crystals. We establish two criteria for this class of crystal: First, theoretically calculated or experimentally derived λ_{PM} based on refractive index dispersion equation is equal (or infinitely close) to its $\lambda_{cut-off}$. Second, it can still achieve the direct harmonic light output when the crystal transmittance is as low as $\sim 0.02\%$. In our previous work¹⁸, two new guanidinium fluorooxoborates were found to have large birefringences (calculated $\Delta n = 0.173$ and 0.161 at 1,064 nm). Such birefringences are sufficient to meet the phase-matching requirement across their whole transparent regions, and λ_{PM} could theoretically be close to their $\lambda_{cut-off}$ using the direct frequency-doubling technique. Unfortunately, both crystallize in the triclinic system, and it is hard to experimentally confirm their laser output ability in the whole transparent region. In this work, a theoretical model was developed and metal-free crystals were highlighted for finding the full-wavelength phase-matching crystals. Based on this, guanidinium tetrafluoroborate ($C(NH_2)_3BF_4$ or GFB) is experimentally found to be able to output frequency-doubling light close to its $\lambda_{cut-off}$.

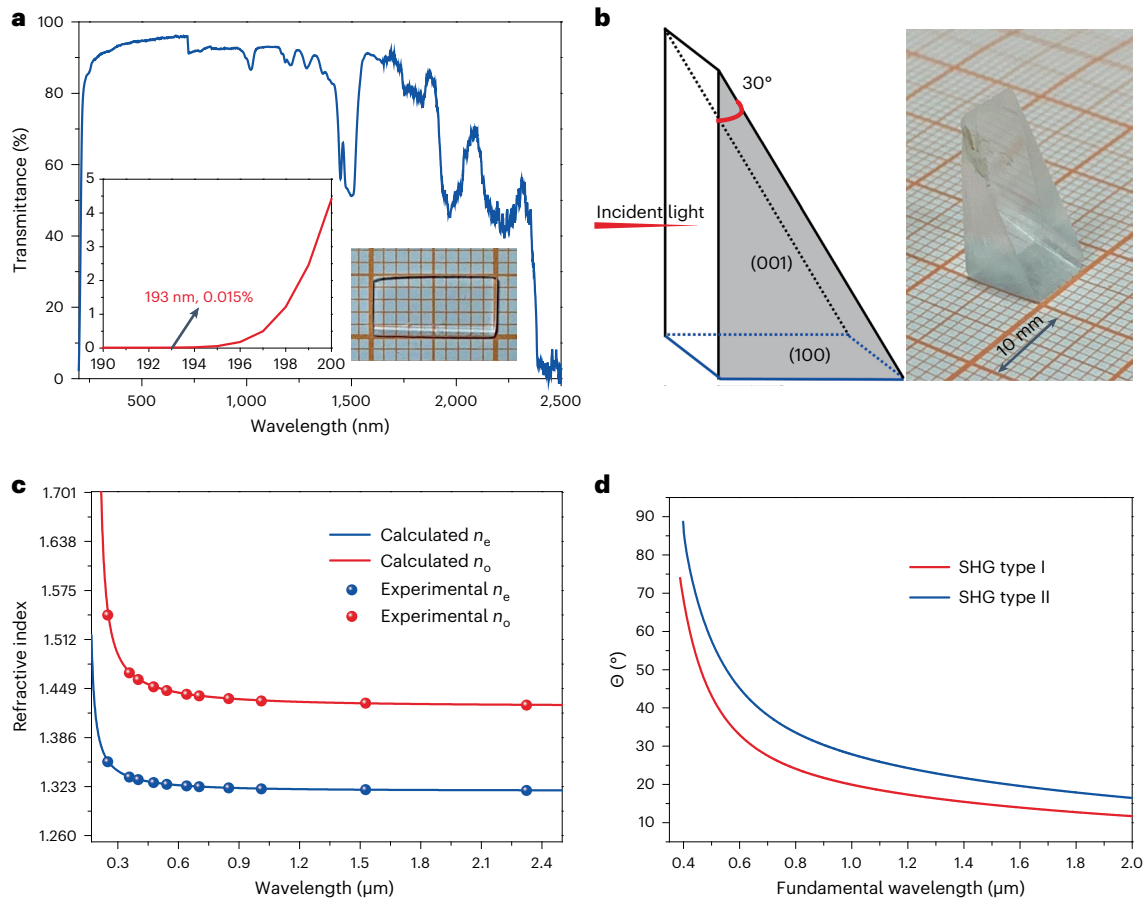


Fig. 2 | Linear and nonlinear optical properties of GFB crystal. a, Transmission spectra of the GFB crystal. The insets represent an enlarged spectral region of 190–200 nm (left) and an as-used GFB crystal plate (right). The vertical fluctuation near 720 nm is caused by a change in light source. **b**, Sketch map (left) and photograph (right) of GFB crystal wedge for the refractive index

characterization. **c**, The refractive index dispersion curves for the GFB crystal: experimental data are expressed as filled dots and calculated data are fitted using pentaparametric Sellmeier equations for n_e and n_o . **d**, Type I and II phase-matching curves of the SHG process for the GFB crystal: type I and II phase-matching occur when $n_o(\omega) = n_e(2\omega)$ and $[n_o(\omega) + n_e(\omega)]/2 = n_e(2\omega)$, respectively.

Results and discussion

Evaluation parameters for full-wavelength phase-matching crystals

First, we show that, from a purely optical perspective, a full-wavelength phase-matching crystal should satisfy the following inequality based on the phase-matching conditions, as well as the dispersion relation between the refractive index (and birefringence) and wavelength:

$$f(\lambda) = \lim_{\lambda \rightarrow 2\lambda_{\text{cut-off}}} \left(\frac{\Delta n(\lambda)}{n_i(\frac{\lambda}{2}) - n_i(\lambda)} \right) \gg 1 \quad (1)$$

Second, we reveal the essence of the refractive index by the derivation of polarization with respect to the field strength. For crystals with ignorable spin-orbital coupling, both the frequency-dependent dielectric tensor ϵ and refractivity n are diagonal. If the four-fold rotation symmetry is preserved then the refractivity tensor has only two elements, n_x and n_z . For crystals with a relatively strong valence bond, the refractivity tensor usually exhibits a relatively large variation with frequency. Nevertheless, it is still possible to design a crystal with one element (for example, n_z) that is almost frequency independent. The low-energy-band dispersion of semiconductors near the Fermi level can usually be mimicked by a massive Dirac electron. From this ground state, we can prove that the refractivity index $n_{i=x,y,z}$ in a wide-bandgap insulator is proportional to the strength of binding γ_i (see Methods

for a detailed derivation process), which characterizes the anisotropic orbital hybridization. On this basis, the refractivity index at low frequency reads

$$n_{ii}(\omega) - 1 = \frac{\gamma_i}{\hbar\omega + E_g} - \frac{\gamma_i}{\hbar\omega - E_g} \propto \frac{\gamma_i}{E_g} \quad (2)$$

When considering the condition of type-I phase-matching for the SHG process for negative uniaxial crystals, that is, $n_{xx}(\omega) = n_{zz}(2\omega)$, it follows that

$$1 + \frac{\gamma_x}{\hbar + E_g} - \frac{\gamma_x}{\hbar\omega - E_g} = 1 + \frac{\gamma_z}{2\hbar\omega + E_g} - \frac{\gamma_z}{2\hbar\omega - E_g} \quad (3)$$

$$\frac{\gamma_x}{\gamma_z} = \frac{(\hbar\omega)^2 - E_g^2}{(2\hbar\omega)^2 - E_g^2} \quad (4)$$

As we proposed that a full-wavelength phase-matching crystal should satisfy the ideal state of $\lambda_{\text{PM}} \rightarrow \lambda_{\text{cut-off}}$, that is, $2\hbar\omega \rightarrow E_g$, which, based on equation (4), leads to a large value of $\frac{\gamma_x}{\gamma_z}$, we can therefore predict that one with a larger $\frac{\gamma_x}{\gamma_z}$ exhibits better phase-matching ability. From a chemical point of view, chemical bonding strength along different principal axes in such crystals should be anisotropic because parameter γ_i is determined by the chemical bond strength. In particular, if

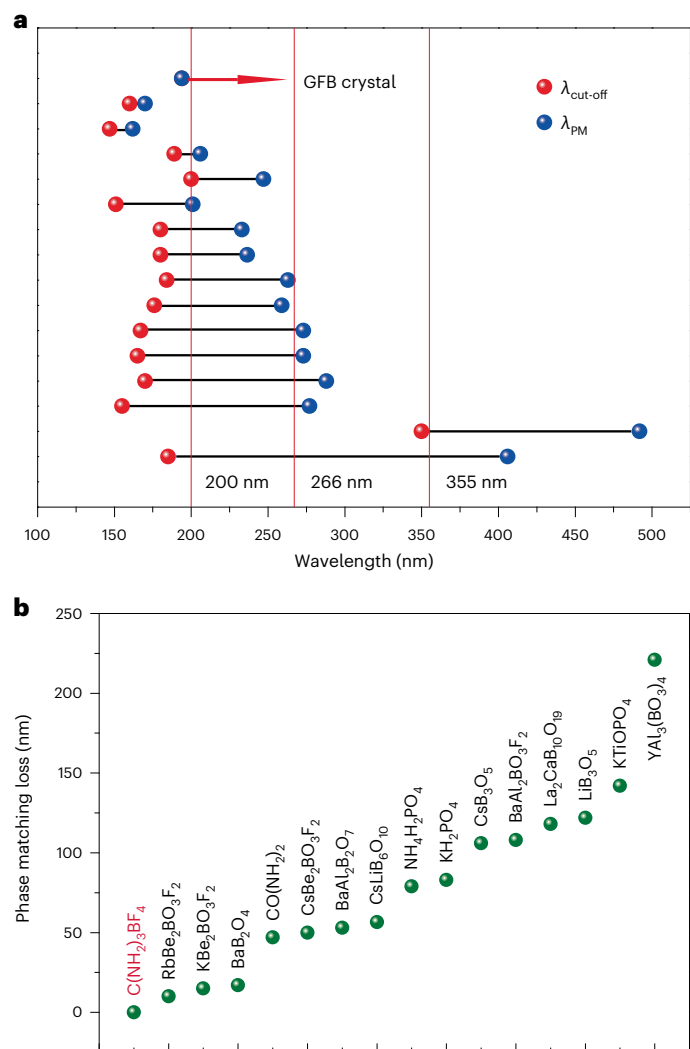


Fig. 3 | Comparison of ultraviolet cut-off edge, shortest phase-matching wavelength and phase-matching wavelength loss. a, Comparisons of the ultraviolet cut-off edge (red spheres) and type I SHG shortest phase-matching wavelength (blue spheres) between representative NLO crystals and GFB. Note that GFB is the only NLO crystal for which the type I SHG shortest phase-matching wavelength is equal to its ultraviolet cut-off edge; GFB is therefore identified as a full-wavelength phase-matching crystal, so far, for a direct SHG process. **b**, Comparisons of the losses (expressed as $\Delta\lambda_l = \lambda_{PM} - \lambda_{cut-off}$) between representative NLO crystals with GFB, in which phase-matching wavelength loss is obvious for NLO oxides applied to various spectral regions in the SHG phase-matching condition; however, such a loss does not exist for GFB. Note that the order of the crystals shown in **a** from top to bottom corresponds to those in **b** from left to right.

$\gamma_z \rightarrow 0$ then n_z is almost frequency independent. This dispersionless refractivity will implement the phase-matching in a wide optical transparency range. For finite γ_x , the crystal should present a large $\frac{\gamma_x}{\gamma_z}$ ratio.

Screening potential full-wavelength phase-matching crystals

On the basis of the above, the following structural features are ideal for potential full-wavelength phase-matching crystals with a large $\frac{\gamma_x}{\gamma_z}$: (1) strong covalently bonded units in the intralayer, and (2) weak interlayer bonds to act on $\gamma_x(\uparrow)$ and $\gamma_z(\downarrow)$. Depending on the circumstances, metal-free crystals might be preferable as the strong covalently bonded units and weak interlayer interactions naturally occur. Furthermore, to achieve highly linear and NLO properties for practical applications, structures with: (1) a uniaxial system, (2) planar units in preferential

arrangement, (3) components free of d - d or f - f electronic transitions, (4) a habit of good growth and (5) high stability and durability, are preferred^{19–28}. We therefore selected GFB which, although a known structure^{29–31}, has not had its linear and nonlinear properties fully studied since it was first discovered in 1987 by Haussühl and co-workers²⁹, especially at the bulk crystal level.

This crystal is constructed by the planar π -conjugated $[C(NH_2)_3]$ units extended in the (001) plane, which are separated by interlaid $[BF_4]$ units (Fig. 1a and Supplementary Fig. 1). The strong covalent C–N bonding within $[C(NH_2)_3]$ is clearly identified from the accumulation of the charge around each atom (Fig. 1b,c and Supplementary Fig. 2). All of the boron atoms at 3a Wyckoff positions of the atomic site are also found to form covalent bonds with fluorine atoms though the same atoms at 3a Wyckoff positions, forming covalent bonds with fluorine to form $[BF_4]$ units; however, the strength is weaker than that of C–N bonds in $[C(NH_2)_3]$, which is evident from the calculated Mulliken bond population (Supplementary Tables 1 and 2)³² and detailed quantum chemical calculations performed by Murugakoothan and colleagues³³. The molecular electrostatic potential contour maps demonstrate the intermolecular interactions in GFB³³. By contrast, weak hydrogen bonds are observed between $[C(NH_2)_3]$ and $[C(NH_2)_3]$ as well as $[C(NH_2)_3]$ and $[BF_4]$ due to the small charge accumulation around them. The field strength-dependent refractive indices are shown in Fig. 1d. A considerable difference between n_{xx} and n_{zz} is observed, especially in the regions close to the band gap where n_{xx} increases suddenly and n_{zz} curves remain relatively flat, indicating a large value of $\frac{\gamma_x}{\gamma_z}$. Meanwhile, the calculated electrostatic potential in real space is not parabolic due to broken spatial inversion symmetry, as shown in Fig. 1e and Supplementary Fig. 3. The electrostatic potential of $[C(NH_2)_3]$ units along the z -axis is shown to be closely related to length, with the minimum and maximum electrostatic potential values achieved next to the axial $[BF_4]$ and $[C(NH_2)_3]$ groups (Fig. 1e and Supplementary Fig. 3). Theoretically calculated refractive index and birefringence of GFB also confirmed that inequality shown in Supplementary Fig. 4 is tenable, showing that birefringence could always compensate the refractive index dispersion for GFB.

Demonstration of the full-wavelength phase-matching ability

Based on the above, GFB might theoretically be a full-wavelength phase-matching crystal in which the phase-matching wavelength fully covers its optical transparency range. Centimetre-scale single crystals (Fig. 1f,g, and Supplementary Tables 3 and 4) were grown and subjected to performance characterization to confirm this (see Supplementary Information for details). Of course, we first determined two key parameters: $\lambda_{cut-off}$ and λ_{PM} . The GFB crystal is characterized by a wide transparency window, displaying a high transmittance (>80%) from 220–1,400 nm with a short $\lambda_{cut-off}$ of ~193 nm (0.015%) (Fig. 2a). As demonstrated in Fig. 2b,c and Supplementary Table 5, GFB is an optically negative uniaxial crystal with a high birefringence in the measured wavelength range. The experimentally determined values were fitted by pentaparametric Sellmeier equations (where e and o represent extraordinary and ordinary rays of light, respectively); the results are as follows:

$$n_e^2 = 2.085820 + \frac{0.008154}{\lambda^2 - 0.037633} - \frac{0.050671\lambda^2}{\lambda^2 + 0.326762}$$

$$n_o^2 = 1.772467 + \frac{0.003144}{\lambda^2 - 0.023015} - \frac{0.035929\lambda^2}{\lambda^2 + 0.124942}$$

Past studies have shown that λ_{PM} is restricted by birefringence¹³, which is the primary factor to be considered. Here we propose that $\frac{\gamma_x}{\gamma_z}$ also influences λ_{PM} and, to further verify this, $CO(NH_2)_2$ (ref. 34), β - BaB_2O_4 (β -BBO)³⁵ and GFB were selected as they have similar birefringences (~0.11 at 1,064 nm), which therefore excludes the variability of

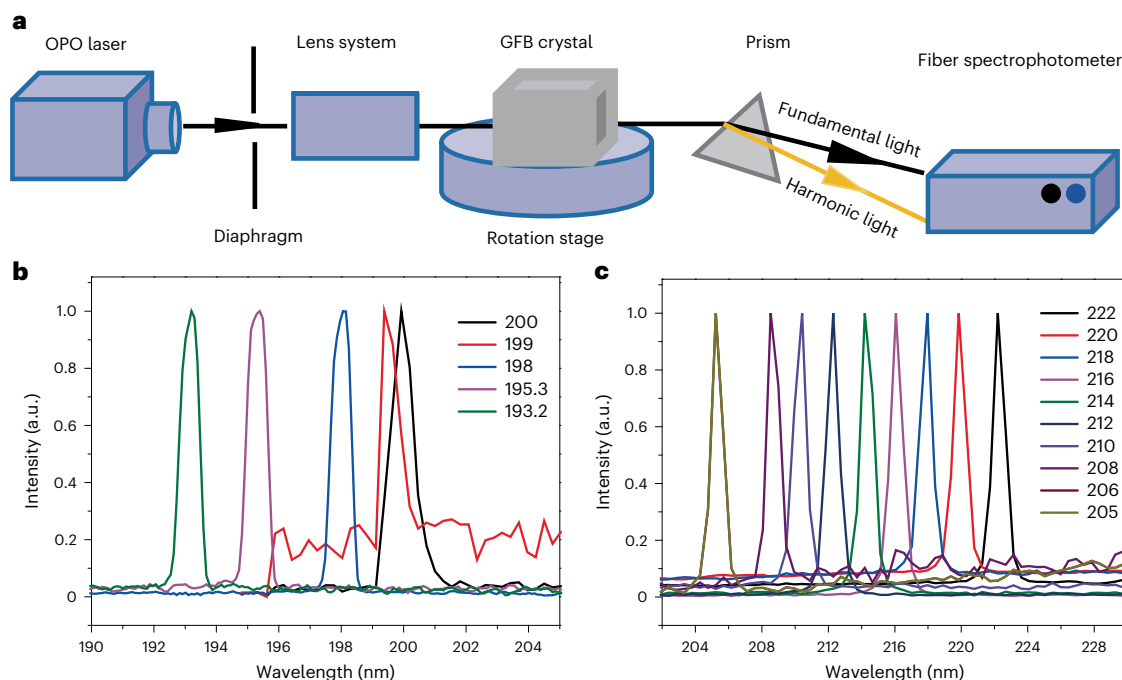


Fig. 4 | Tunable harmonic light generation of GFB crystal. **a**, The experimental settings for the generation of tunable 193.2–266 nm light, in which the coherent light source can be provided by frequency-doubled titanium:sapphire laser (for the generation of tunable 193.2–200 nm light) and 355 nm-pumped nanosecond optical parametric oscillation (OPO) (for the generation of tunable 205–266 nm light). **b,c**, Observation of frequency-doubling light using the different GFB

crystals, that is: $(\theta, \phi) = (64.44^\circ, 90^\circ)$ for 193.2–200 nm light generation (**b**), $(\theta, \phi) = (54.03^\circ, 90^\circ)$ for 205–222 nm light generation (**c**) and $(\theta, \phi) = (39.12^\circ, 90^\circ)$ for 236–266 nm light generation (see Supplementary Fig. 5). Note that the SHG intensity is normalized for a better version, and the raw data are available in Supplementary Figs. 6–9.

birefringence and focuses on the influence of $\frac{y_x}{y_z}$ on λ_{PM} . As such, the $\frac{y_x}{y_z}$ ratios at the λ_{PM} wavelengths for $\text{CO}(\text{NH}_2)_2$, β -BBO and GFB were calculated to be 2.46, 5.25 and $+\infty$, respectively. The size relation is consistent with the loss of $\Delta\lambda_l$ (that is, 46, 16 and 0 nm), indicating that, under the premise of having similar birefringence, larger $\frac{y_x}{y_z}$ causes lower loss of phase-matching wavelength. This might provide a new insight for searching NLO crystals with wide phase-matching wavelength.

The phase-matching curves (Fig. 2d) for SHG are determined on the basis of the Sellmeier equations: type I and II phase-matching occur when $n_o(\omega) = n_e(2\omega)$ and $[n_o(\omega) + n_e(\omega)]/2 = n_e(2\omega)$, respectively^{1,2,13}. GFB can achieve SHG phase-matching for both type I and II in the main directions, and λ_{PM} for type I is down to ~ 194 nm, in sync with its $\lambda_{\text{cut-off}}$. This indicates that GFB can, in principle, be phase-matchable across its whole optical transparency range, unlike other NLO crystals. We compare $\Delta\lambda_l$ values between representative NLO crystals and GFB in Fig. 3a,b, in which phase-matching wavelength loss is obvious for NLO oxides applied to various spectral regions in the SHG phase-matching condition; nevertheless, there is no loss in GFB. We performed the frequency-doubling experiment using three different GFB crystals to verify this. The tunable frequency-doubled light output has been achieved from 193.2 to 266 nm (Fig. 4a–c and Supplementary Figs. 5–9), indicating that GFB is able to output frequency-doubling light close to its $\lambda_{\text{cut-off}}$ and is therefore identified as a full-wavelength phase-matching crystal for a direct SHG process. It should be noted that GFB can still achieve the direct harmonic light output when its transmittance at 193.2 nm is lower than 0.02%, demonstrating its full-wavelength phase-matching ability. Successful output of 193.2 nm deep-ultraviolet light makes GFB the third NLO crystal that is already capable of generating deep-ultraviolet light below 200 nm with direct SHG technology^{17,19,36}. Unlike GFB, owing to the unobtainable large single crystals caused by the strong layer growth tendency, a prism-coupled device is essential for other two sole deep-ultraviolet NLO crystals $\text{ABe}_2\text{BO}_3\text{F}_2$ (where A = K and Rb)³⁶.

Optical performance evaluation and 266 nm light generation ability

Solid-state lasers emitting at 266 nm are also used in various applications, and such emission can be achieved from commercially available laser sources (including a Nd:YAG laser with a wavelength of 1,064 nm) via a multifrequency conversion process using NLO crystals^{14,35–44}. So far, three main NLO crystals are currently commercially available for fourth-harmonic generation (FHG) of a Nd:YAG laser, namely KH_2PO_4 (KDP)³⁷, β -BBO³⁵ and $\text{CsLiB}_6\text{O}_{10}$ (CLBO)^{38,39}, but some practical inherent drawbacks limit their applications. By contrast, GFB could be a high-performance crystal for FHG at 266 nm, and its advantages are mainly demonstrated in the following aspects. First, they exhibit reproducible, easy growth of sizeable bulk single crystals, and are green and low cost. They can be grown by a simple solution-growth technique⁴⁵—one of the most developed and widely used approaches—and dimensions of $40 \times 30 \times 21$ mm³ were achieved during the first attempt in the laboratory (Fig. 1f,g). A larger size is expected to be obtainable as the technique for growing classic NLO crystals, including KDP—by which the largest crystals known to mankind have been grown—can be referenced³⁷. Furthermore, the growth temperature ($\sim 40^\circ\text{C}$) is low and the guanidine carbonate and tetrafluoroboric acid raw materials are cheap to buy. Accordingly, compared with the available NLO crystals for FHG of 266 nm light, the growth of GFB is easier, greener and less expensive. Second, GFB exhibits high transmittance at 266 nm, a high laser-induced damage threshold and low thermal expansion anisotropy. The transmittance at 266 nm of GFB crystal is as high as 88.9% (Fig. 2a), which is comparable with that of KDP (89.1%) and β -BBO (88.6%) crystals under the same experimental conditions. The laser-induced damage threshold of 0.36 and 2.18 GW cm^{-2} is measured for a GFB crystal, which is higher than that of β -BBO (0.32 and 1.93 GW cm^{-2}) and KD_2P_4 (DKDP, 0.21 and 1.12 GW cm^{-2}) crystals under the same conditions (5 ns, 10 Hz, 266/532 nm). The average thermal expansion coefficients are evaluated to be $\alpha_a = \alpha(100) = 11.04 \times 10^{-5} \text{ K}^{-1}$ and $\alpha_c = \alpha(001) = 14.64 \times 10^{-5} \text{ K}^{-1}$,

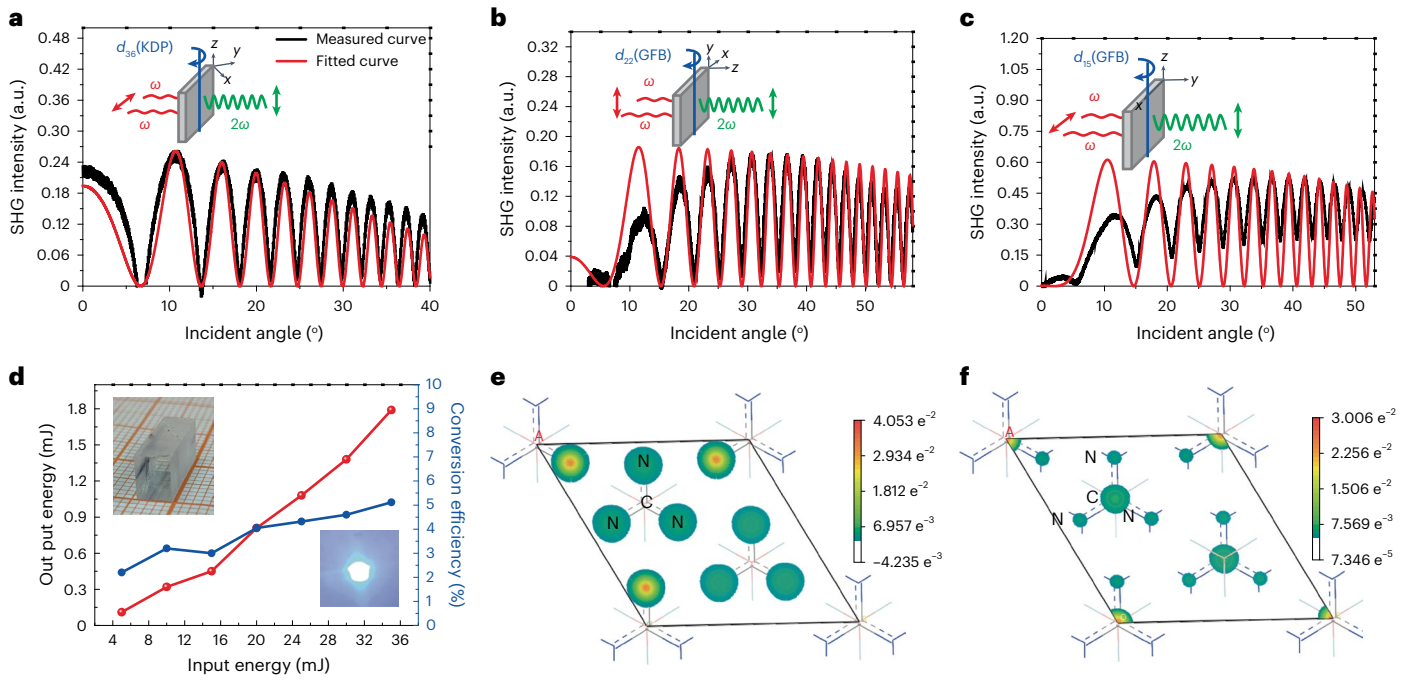


Fig. 5 | Second-order NLO coefficients and structure–property relationship analysis. **a–c.** The orientations (insets), and measured and calculated Maker fringe data for KDP reference and GFB crystal plates, for measuring the NLO coefficients of d_{36} (KDP) (**a**), d_{22} (GFB) (**b**) and d_{15} (GFB) (**c**). The data were fitted according to the Maker fringe theory; the fitting procedure is available in the Supplementary Information. **d.** The input energy at 532 nm versus the output energy at 266 nm, and corresponding conversion efficiency of a GFB crystal from 532 to 266 nm. Insets show the device ($4 \times 5 \times 12.3 \text{ mm}^3$, $(\theta, \phi) = (39.12^\circ$,

90°); upper left) and output 266 nm laser spot (lower right) for this experiment. The experimental setting for 266 nm laser light generation is shown in Supplementary Fig. 14. **e, f.** The electron localization function diagrams slice along the ab plane viewed down from z -axis for the occupied (**e**) and unoccupied (**f**) states of the virtual electron for d_{22} (GFB). The isovalue increases from white to red with the region from -4.235×10^{-3} to 4.053×10^{-2} (occupied state) and 7.346×10^{-5} to 3.006×10^{-2} (unoccupied state).

respectively (Supplementary Fig. 10). The α/α_3 ratio is about 1.3, which is much smaller than that of β -BBO (9.0)³⁴ and close to those of CLBO (1.3)^{38,39} and KDP (1.37)³⁷, suggesting that GFB has a favourable anisotropic thermal expansion. Furthermore, Nandhini et al.³¹ suggested that GFB is a soft material, which will effectively protect the crystals from cracking. This is verified by the processing stability of GFB crystal when it was cut into different wafers and no cracks were found. Third, GFB has a high nonlinear optical coefficient. GFB crystallizes in the polar space group $R3m$ that belongs to point group $3m$ with three non-zero independent second-order NLO coefficients^{1,2}. We measured d_{15} and d_{22} by the Maker fringes technology as d_{33} is excluded from the formula for effective second-order NLO coefficient (d_{eff})^{1,2,13}:

$$d_{\text{eff}}^I = d_{\text{ooe}} = d_{15} \sin \theta - d_{22} \cos \theta \sin 3\varphi \quad (5)$$

$$d_{\text{eff}}^{II} = d_{\text{oeo}} = d_{22} \cos^2 \theta \cos 3\varphi \quad (6)$$

In which θ is the angle between the wave vector and z -axis, and φ is the angle between the projection of the wave vector in the XY plane and Z axis. The GFB crystals were cut in phase-matching directions (θ_{PM}) for both phase-matching conditions with two different configurations corresponding to propagation in the XZ and YZ planes, respectively. This leads to the following formula transformation and the distributions of $|d_{\text{eff}}|$ and θ_{PM} under different types of phase-matching conditions and main plane are shown in Supplementary Fig. 11.

$$d_{\text{eff},I}^{XZ} = d_{15} \sin \theta_{\text{PM}} (\varphi = 0^\circ) \quad (7)$$

$$d_{\text{eff},I}^{YZ} = d_{15} \sin \theta_{\text{PM}} + d_{22} \cos \theta_{\text{PM}} (\varphi = 90^\circ) \quad (8)$$

$$d_{\text{eff},II}^{XZ} = d_{22} \cos^2 \theta_{\text{PM}} (\varphi = 0^\circ) \quad (9)$$

$$d_{\text{eff},II}^{YZ} = 0 (\varphi = 90^\circ) \quad (10)$$

It should be emphasized that the signs of d_{15} and d_{22} are different based on complete neglect of differential overlap approximation and the anionic group theory¹⁹. Thus, according to the measurements and calculations (see Supplementary Fig. 12 and the 'Experimental' section of the Supplementary Information), the NLO coefficients of GFB crystal relative to d_{36} (KDP) have been determined to be $d_{22} = \pm 4.03 \times d_{36}$ (KDP) and $d_{15} = \mp 1.95 \times d_{36}$ (KDP), respectively (Fig. 5a–c). As d_{36} (KDP) is equal to 0.39 pm V^{-1} at 1,064 nm (ref. 37), the absolute NLO coefficients for GFB crystal are $|d_{22}| = 1.57 \text{ pm V}^{-1}$ and $|d_{15}| = 0.76 \text{ pm V}^{-1}$, and the size relation is consistent with the pure theoretical results under 1,064 nm (-1.17 eV) (Supplementary Fig. 13). Thus, absolute experimental $|d_{\text{eff}}|$ under different conditions reads $|d_{\text{eff},I}^{XZ}| = 0.25 \text{ pm V}^{-1}$, $|d_{\text{eff},II}^{YZ}| = 1.24 \text{ pm V}^{-1}$, $|d_{\text{eff},II}^{XZ}| = 1.40 \text{ pm V}^{-1}$ and $|d_{\text{eff},II}^{YZ}| = 0 \text{ pm V}^{-1}$, in which the phase-matching angle θ_{PM} is 19° at 1,064 nm. Importantly, the $|d_{\text{eff},II}^{XZ}|$ and $|d_{\text{eff},I}^{YZ}|$ values of the GFB crystal are about 5.38/4.77- and 3.68/3.26-times greater than those of KDP ($|d_{\text{eff}}| = 0.26 \text{ pm V}^{-1}$)³⁷ and CLBO ($|d_{\text{eff}}| = 0.38 \text{ pm V}^{-1}$)³⁹, respectively, and comparable with that of a β -BBO crystal (1.75 pm V^{-1})³⁶.

We next verify the 266 nm light generation ability using an optically polished GFB crystal (upper-left inset, Fig. 5d) for type I phase-matching ($o + o \rightarrow e$). The schematic set-up for 266 nm light generation is shown in Supplementary Fig. 14, whereas Supplementary Figs. 15 and 16 provide a discussion on the walk-off angles. GFB exhibits a walk-off angle that is about 1.2 times higher than that of β -BBO for a type I SHG ($o + o \rightarrow e$) with a 532 \rightarrow 266 nm interaction. A blue bright spot—identified as a 266 nm

laser spot—was clearly observed and recorded, as shown in Fig. 5d. For a quantitative characterization of 266 nm light generation ability, we recorded an output energy at 266 nm for different input energy at 532 nm and the results are shown in Fig. 5d. An output energy of 1.78 mJ was obtained with an SHG conversion efficiency of 5.1%. Although this is considerable data for a new NLO crystal when it was confirmed for the first time to have the potential of generating 266 nm light, and its output energy and conversion efficiency can, in principle, be further improved in future works.

Clarification of nonlinear optical response origin

Theoretically, the SHG origin of GFB was investigated from the perspective of orbital analysis using the SHG density method⁴⁶. The contributions of the virtual electron process to SHG tensors are larger than those of the virtual hole process, indicating that the SHG effects of GFB mainly originate from the former. Thus, only the virtual electron process for the largest SHG tensor (d_{22}) is analysed and the results are displayed in Fig. 5e,f and Supplementary Fig. 17. The SHG density completely originates from non-bonding $2p$ orbitals of nitrogen and carbon in π -conjugated $[\text{C}(\text{NH}_2)_3]$ modules in GFB, whereas in the virtual electron unoccupied state, it mainly comes from the $2p$ orbitals of nitrogen and carbon in π -conjugated $[\text{C}(\text{NH}_2)_3]$ units, with also a small contribution from $2p$ orbitals of boron and fluorine in non- π -conjugated $[\text{BF}_4]$ tetrahedra. Furthermore, to investigate the contribution of the respective units (that is, $[\text{C}(\text{NH}_2)_3]$ and $[\text{BF}_4]$ units) on NLO coefficients of GFB, a real-space atom-cutting method was adopted⁴⁷. This suggests that the contribution of d_{22} from non- π -conjugated $[\text{BF}_4]$ is small (Supplementary Table 6); instead, the main contribution comes from the π -conjugated $[\text{C}(\text{NH}_2)_3]$ units. When taken together, we concluded that the π -conjugated $[\text{C}(\text{NH}_2)_3]$ modules are responsible for the SHG coefficient of d_{22} and thus it can be regarded as the NLO-active chromophore. From a deeper view, we studied the charge transfer between $[\text{BF}_4]$ and $[\text{C}(\text{NH}_2)_3]$. The calculated band structure (Supplementary Figs. 18 and 19) demonstrates that the valence bands are dominated by the $2p$ orbitals from fluorine atoms and nitrogen atoms, while the conducting band is dominated by the $2s$ orbitals of carbon atoms. There are thus two channels for charge transfer under a light field: between F–C or N–C. We note that $[\text{C}(\text{NH}_2)_3]$ is highly symmetric, whereas $[\text{BF}_4]$ derives from the centre of two neighbouring $[\text{C}(\text{NH}_2)_3]$ units. We conclude that the charge transfers between $[\text{BF}_4]$ and $[\text{C}(\text{NH}_2)_3]$ are responsible for the SHG in this crystal. From the shift vector, the calculated SHG coefficients (Supplementary Fig. 13) also show that the photon energy of two-photon resonance (single-photon resonance) is slightly higher than $E_g/2(E_g)$, which also supports that charge transfer between $[\text{BF}_4]$ and $[\text{C}(\text{NH}_2)_3]$ is the dominating mechanism for the SHG in GFB.

Conclusion

We clarified the role of the anisotropic strength of bonding in the dimension of energy on phase-matching wavelength and, based on this, we proposed a new class of materials: full-wavelength phase-matching crystals, which hold the ability to generate frequency doubling light within their whole optical transparency range. Tunable frequency-doubled light output was achieved from 193.2–266 nm, which indicates that GFB can output frequency doubling light close to its $\lambda_{\text{cut-off}}$ and therefore it is identified as a full-wavelength phase-matching crystal for a direct SHG process. A large GFB crystal enables us to make a careful evaluation of its ability for FHG at 266 nm. We here summarize the main findings. First, reproducible easy growth of sizeable bulk single crystals using a simple solution growth technique, which leads to the successful growth of large crystals. Second, the transmittance at 266 nm of GFB crystal is as high as 88.9%. GFB exhibits a favourable anisotropic thermal expansion with an α_c/α_a ratio of only 1.3, which will effectively protect the crystals from cracking. Third, the GFB has large NLO coefficients of $|d_{\text{eff},1}^{\text{YZ}}| = 1.24 \text{ pm V}^{-1}$ and $|d_{\text{eff},1}^{\text{XZ}}| = 1.40 \text{ pm V}^{-1}$. Finally, a considerable output energy of 1.78 mJ at

266 nm was obtained with a SHG process. We believe that our results will drastically drive the discovery of more full-wavelength phase-matching crystals with distinctive optical properties.

Online content

Any methods, additional references, Nature Portfolio reporting summaries, source data, extended data, supplementary information, acknowledgements, peer review information; details of author contributions and competing interests; and statements of data and code availability are available at <https://doi.org/10.1038/s41566-023-01228-7>.

References

- Bloembergen, N. *Nonlinear Optics* (World Scientific, 1996).
- Boyd, R. W. *Nonlinear Optics* (Academic, 2008).
- Nielsen, M. P., Shi, X. Y., Dichtl, P., Maier, S. A. & Oulton, R. F. Giant nonlinear response at a plasmonic nanofocus drives efficient four-wave mixing. *Science* **358**, 1179–1181 (2017).
- Klimmer, S. et al. All-optical polarization and amplitude modulation of second-harmonic generation in atomically thin semiconductors. *Nat. Photon.* **15**, 837–842 (2021).
- Beetar, J. E. et al. *Sci. Adv.* **6**, eabb5375 (2020).
- Armstrong, J. A., Bloembergen, N., Ducuing, J. & Pershan, P. S. Light waves at the boundary of nonlinear media. *Phys. Rev.* **127**, 1918–1939 (1962).
- Suchowski, H. et al. Phase mismatch-free nonlinear propagation in optical zero-index materials. *Science* **342**, 1223–1226 (2013).
- Zhu, S. N., Zhu, Y. Y. & Ming, N. B. Quasi-phase-matched third-harmonic generation in a quasi-periodic optical superlattice. *Science* **278**, 843–846 (1997).
- Fiore, A., Berger, V., Rosencher, E., Bravetti, P. & Nagle, J. Phase matching using an isotropic nonlinear optical material. *Nature* **391**, 463–466 (1998).
- Lan, S. F. et al. Backward phase-matching for nonlinear optical generation in negative-index materials. *Nat. Mater.* **14**, 807–811 (2015).
- Shao, M. C., Liang, F., Yu, H. H. & Zhang, H. J. Pushing periodic-disorder-induced phase matching into the deep-ultraviolet spectral region: theory and demonstration. *Light: Sci. Appl.* **9**, 45 (2020).
- Bahabad, A., Cohen, O., Murnane, M. & Kapteyn, H. Quasi-periodic and random quasi-phase matching of high harmonic generation. *Opt. Lett.* **33**, 1936–1938 (2008).
- Zhang, W. G., Yu, H. W., Wu, H. P. & Halasyamani, P. S. Phase-matching in nonlinear optical compounds: a materials perspective. *Chem. Mater.* **29**, 2655–2668 (2017).
- Nikogosyan, D. N. *Nonlinear Optical Crystals: A Complete Survey* (Springer Science, 2009).
- Trabs, P., Noack, F., Aleksandrovsky, A. S., Zaitsev, A. I. & Petrov, V. Generation of coherent radiation in the vacuum ultraviolet using randomly quasi-phase-matched strontium tetraborate. *Opt. Lett.* **41**, 618–621 (2016).
- Wei, D. Z. et al. Efficient nonlinear beam shaping in three-dimensional lithium niobate nonlinear photonic crystals. *Nat. Commun.* **10**, 4193 (2019).
- Mutailipu, M. & Pan, S. L. Emergent deep-ultraviolet nonlinear optical candidates. *Angew. Chem. Int. Ed.* **59**, 20302–20317 (2020).
- Jin, C. C. et al. Guanidinium fluorooxoborates as efficient metal-free short-wavelength nonlinear optical crystals. *Chem. Mater.* **34**, 440–450 (2022).
- Chen, C. T. et al. *Nonlinear Optical Borate Crystals: Principles and Applications* (Wiley-VCH, 2012).
- Mutailipu, M., Poepelmeier, K. R. & Pan, S. L. Borates: a rich source for optical materials. *Chem. Rev.* **121**, 1130–1202 (2021).

21. Ok, K. M. Toward the rational design of novel noncentrosymmetric materials: factors influencing the framework structures. *Acc. Chem. Res.* **49**, 2774–2785 (2016).
22. Luo, M., Ye, N., Zou, G. H., Lin, C. S. & Cheng, W. D. $\text{Na}_8\text{Lu}_2(\text{CO}_3)_6\text{F}_2$ and $\text{Na}_3\text{Lu}(\text{CO}_3)_2\text{F}_2$: rare earth fluoride carbonates as deep-UV nonlinear optical materials. *Chem. Mater.* **25**, 3147–3153 (2013).
23. Kang, L., Liang, F., Jiang, X. X., Lin, Z. S. & Chen, C. T. First-principles design and simulations promote the development of nonlinear optical crystals. *Acc. Chem. Res.* **53**, 209–217 (2020).
24. Mutailipu, M. et al. L Strong nonlinearity induced by coaxial alignment of polar chain and dense $[\text{BO}_3]$ units in $\text{CaZn}_2(\text{BO}_3)_2$. *Angew. Chem. Int. Ed.* **61**, e202202096 (2022).
25. Kong, F., Huang, S. P., Sun, Z. M., Mao, J. G. & Cheng, W. D. $\text{Se}_2(\text{B}_2\text{O}_7)$: a new type of second-order NLO material. *J. Am. Chem. Soc.* **128**, 7750–7751 (2006).
26. Aka, G. et al. Linear- and nonlinear-optical properties of a new gadolinium calcium oxoborate crystal, $\text{Ca}_4\text{GdO}(\text{BO}_3)_3$. *J. Opt. Soc. Am. B* **14**, 2238–2247 (1997).
27. Oganov, A. R., Pickard, C. J., Zhu, Q. & Needs, R. J. Structure prediction drives materials discovery. *Nat. Rev. Mater.* **4**, 331–348 (2019).
28. Knyrim, J. S., Becker, P., Johrendt, D. & Huppertz, H. A new non-centrosymmetric modification of BiB_3O_6 . *Angew. Chem. Int. Ed.* **45**, 8239–8241 (2006).
29. Krumbel, W. & Haussühl, S. Crystal culture and determination of structure for guanidinium-hydrogen-selenite, guanidinium-hydrogen-phosphite, guanidinium-tetrafluoroborate, guanidinium-glutarate and guanidinium-acetate. *Z. Kristallogr.* **178**, 132–134 (1987).
30. Haussühl, S. Pyroelectric, dielectric, piezoelectric, and elastic properties of trigonal guanidinium tetrafluoroborate, $\text{C}(\text{NH}_2)_3\text{BF}_4$. *Z. Kristallogr.* **187**, 153–158 (1989).
31. Nandhini, S., Sudhakar, K., Muniyappan, S. & Murugakoothan, P. Systematic discussions on structural, optical, mechanical, electrical and its application to NLO devices of a novel semi-organic single crystal: guanidinium tetrafluoroborate (GFB). *Opt. Laser Technol.* **105**, 249–256 (2018).
32. Mulliken, R. S. Electronic population analysis on LCAO–MO molecular wave functions. *J. Chem. Phys.* **23**, 1833–1840 (1955).
33. Nandhini, S., Muniyappan, S., Ramar, S. V., Balasubramanian, K. & Murugakoothan, P. Quantum chemical analysis on supramolecular assemblies of guanidinium tetrafluoroborate (GFB) crystal structure: emission and NLO behavior. *J. Mol. Struct.* **1198**, 126859 (2019).
34. Halbout, J. M. & Tang, C. L. *Nonlinear Optical Properties of Organic Molecules and Crystals* (Academic, 1998).
35. Chen, C. T., Wu, B. C., Jiang, A. D. & You, G. M. A new ultraviolet SHG crystal $\beta\text{-BaB}_2\text{O}_4$. *Sci. Sin., Ser. B* **28**, 235–243 (1985).
36. Xu, Z. Y. et al. Advances in deep ultraviolet laser based high-resolution photoemission spectroscopy. *Front. Inform. Technol. Electron. Eng.* **20**, 885–913 (2019).
37. Eimerl, D. Electro-optic, linear, and nonlinear optical properties of KDP and its isomorphs. *Ferroelectrics* **72**, 95–139 (1987).
38. Mori, Y., Kuroda, I., Nakajima, S., Sasaki, T. & Nakai, S. New nonlinear optical crystal: cesium lithium borate. *Appl. Phys. Lett.* **67**, 1818–1820 (1995).
39. Shoji, I. et al. Absolute measurement of second-harmonic nonlinear optical coefficients of $\text{CsLiB}_6\text{O}_{10}$ for visible-to-ultraviolet second-harmonic wavelengths. *J. Opt. Soc. Am. B* **18**, 302–307 (2001).
40. Sasaki, T., Mori, Y., Yoshimura, M., Yap, Y. K. & Kamimura, T. Recent development of nonlinear optical borate crystals: key materials for generation of visible and UV light. *Mater. Sci. Eng. R* **30**, 1–54 (2000).
41. Xu, K., Loiseau, P. & Aka, G. BaCaBO_3F : a nonlinear optical crystal investigated for UV light generation. *J. Cryst. Growth* **311**, 2508–2512 (2009).
42. Yang, L., Yue, Y. C., Yang, F., Hu, Z. G. & Xu, X. Y. 266 nm ultraviolet light generation in Ga-doped $\text{BaAlBO}_3\text{F}_2$ Crystals. *Opt. Lett.* **41**, 1598–1600 (2016).
43. Xu, K. et al. Nonlinear optical properties of $\text{Ca}_5(\text{BO}_3)_3\text{F}$ crystal. *Opt. Express* **16**, 17735–17744 (2016).
44. Fang, Z. et al. High-efficiency UV generation at 266 nm in a new nonlinear optical crystal $\text{NaSr}_3\text{Be}_3\text{B}_3\text{O}_9\text{F}_4$. *Opt. Express* **25**, 26500–26507 (2017).
45. Dhanaraj, G., Byrappa, K., Prasad V. & Dudley, M. *Springer Handbook of Crystal Growth* (Springer, 2010).
46. Aversa, C. & Sipe, J. E. Nonlinear optical susceptibilities of semiconductors: results with a length-gauge analysis. *Phys. Rev. B* **52**, 14636–14645 (1995).
47. Lin, J., Lee, M. H., Liu, Z. P., Chen, C. T. & Pickard, C. J. Mechanism for linear and nonlinear optical effects in $\beta\text{-BaB}_2\text{O}_4$ crystals. *Phys. Rev. B* **60**, 13380–13389 (1999).

Publisher's note Springer Nature remains neutral with regard to jurisdictional claims in published maps and institutional affiliations.

Springer Nature or its licensor (e.g. a society or other partner) holds exclusive rights to this article under a publishing agreement with the author(s) or other rightsholder(s); author self-archiving of the accepted manuscript version of this article is solely governed by the terms of such publishing agreement and applicable law.

© The Author(s), under exclusive licence to Springer Nature Limited 2023

Methods

Single crystal growth and polycrystalline sample preparation

Guanidine carbonate (900 g, Shanghai Aladdin Biochemical Technology, 99%) and 1,500 ml tetrafluoroboric acid (Shanghai Aladdin Biochemical Technology, 50 wt% in H₂O) were weighed. The weighed guanidine carbonate was then slowly added to tetrafluoroboric acid to release the carbon dioxide. When no gas is produced, the additional deionized water (500 ml) was added to completely dissolve the products. The solution was then filtered and heated to 65 °C and kept at this temperature for 24 h; it was then slowly cooled to room temperature at a rate of 2 °C per hour. GFB crystals were obtained by filtration and then dried at 60 °C. Next, GFB polycrystalline samples (200 g) were weighed, dissolved in 150 ml deionized water and heated to 45 °C and then transferred to a growth trough. After that, the solution was slowly cooled to 41.67 °C (0.2 °C higher than its saturation point of 41.47 °C), and held at this temperature for 24 h. The GFB seed crystal was then immersed to eliminate the surface defects before the growth. The solution system was cooled to 41.47 °C and the rotation rate of the crystal carrier was set as 30 rounds per min, and subsequently slowly cooled to 39.03 °C at a rate of 0.01–0.20 °C per day. With this, a large GFB crystal with the dimension of 40 × 30 × 21 mm³ solution was grown and weighed (15.54 g). Unlike in this work, in which a cooling method was used to grow GFB crystals, a controlled evaporation method was used by Haussühl and co-workers²⁸. The polycrystalline powder samples for experimental characterization were obtained directly by grinding the as-grown crystals, and their purity was checked by X-ray diffraction (Supplementary Fig. 20). The linear and NLO performance characterizations were then performed based on the as-grown crystal, as shown in the Supplementary information. Supplementary Fig. 21 gives the transmission spectra of GFB crystal under different humidity from 10–98% relative humidity. This indicates that GFB crystal is stable in the low humidity environment.

Formula derivation

At static limit, the real refractive index n_i from dipole approximation is proportional to the strength of bonding γ_i . To derive the expression for refractive index, we start from following interacting Hamilton with dipole approximation⁵,

$$h = h_0 + h_1 = h_0 - e \vec{r} \cdot \vec{E}(t), \quad (\text{M1})$$

where $\vec{E}(t)$ is applied optic field, h_0 is the ground Hamiltonian with assumption that the variation of refractive index due to broken spatial inversion symmetry is negligible, and e and r represent elementary charge of electron and position operator, respectively. The density matrix is defined as follows,

$$\rho = |\psi\rangle\langle\psi|, \quad (\text{M2})$$

and satisfies the below equation

$$i\hbar \frac{d\rho}{dt} = [h, \rho]. \quad (\text{M3})$$

The element of density matrix

$$\rho_{nm}(\vec{k}, t) = \langle n(\vec{k}) | \rho(t) | m(\vec{k}) \rangle \quad (\text{M4})$$

satisfies,

$$i\hbar \frac{d\rho_{nm}(k, t)}{dt} = \langle n(\vec{k}) | [h, \rho] | m(\vec{k}) \rangle. \quad (\text{M5})$$

Making use of position element $\langle n(\vec{k}) | \hat{r} | m(\vec{k}) \rangle = \vec{A}_{nm}(\vec{k}) + i\delta_{nm} \partial_{\vec{k}}$, the intra-band element is vanished.

$$\begin{aligned} & \hbar\omega \rho_{nn}^{(1)}(\vec{k}, \omega) \\ &= \langle n(\vec{k}) | h_0 \rho^{(1)} - \rho^{(1)} h_0 | n(\vec{k}) \rangle + \langle n(\vec{k}) | h_1 \rho^{(0)} - \rho^{(0)} h_1 | n(\vec{k}) \rangle \end{aligned} \quad (\text{M6})$$

$$\hbar\omega \rho_{nn}^{(1)}(\vec{k}, \omega) = -ieE(\omega) \cdot \frac{\partial \rho_{nn}^{(0)}(\vec{k})}{\partial \vec{k}} = 0 \quad (\text{M7})$$

$$\begin{aligned} & \hbar\omega \rho_{nm}^{(1)}(\vec{k}, \omega) \\ &= \langle n(\vec{k}) | h_0 \rho^{(1)} - \rho^{(1)} h_0 | m(\vec{k}) \rangle + \langle n(\vec{k}) | h_1 \rho^{(0)} - \rho^{(0)} h_1 | m(\vec{k}) \rangle \end{aligned} \quad (\text{M8})$$

$$(\hbar\omega - \varepsilon_{nm}) \rho_{nm}^{(1)}(\vec{k}, \omega) = \langle n(\vec{k}) | h_1 | m(\vec{k}) \rangle (\rho_{mm}^{(0)}(\vec{k}) - \rho_{nn}^{(0)}(\vec{k})) \quad (\text{M9})$$

The inter-band density matrix reads,

$$\rho_{nm}^{(1)}(\vec{k}, \omega) = \frac{\langle n(\vec{k}) | h_1 | m(\vec{k}) \rangle}{\hbar\omega - \varepsilon_{nm}} (\rho_{mm}^{(0)}(\vec{k}) - \rho_{nn}^{(0)}(\vec{k})) \quad (\text{M10})$$

and the electronic polarization reads,

$$P_i = -\frac{e^2}{(2\pi)^3} E_i \int \frac{A_{nm}^i A_{mn}^i}{\hbar\omega - \varepsilon_{nm}} (\rho_{mm}^{(0)}(\vec{k}) - \rho_{nn}^{(0)}(\vec{k})) d\vec{k}, \quad (\text{M11})$$

where i takes value in x, y, z , V is the volume of unit cell, and

$$\varepsilon_{nm} = \varepsilon_n - \varepsilon_m. \quad (\text{M12})$$

The frequency dependent dielectric function with linear response reads,

$$\varepsilon_{xx} = 1 + \frac{e^2}{(2\pi)^3 \varepsilon_0} \int \frac{A_{nm}^x A_{mn}^x}{\hbar\omega + \varepsilon_{nm}} \rho_{mm}^{(0)}(\vec{k}) d\vec{k} - \frac{e^2}{(2\pi)^3 \varepsilon_0} \int \frac{A_{nm}^x A_{mn}^x}{\hbar\omega - \varepsilon_{nm}} \rho_{nn}^{(0)}(\vec{k}) d\vec{k} \quad (\text{M13})$$

$$\varepsilon_{zz} = 1 + \frac{e^2}{(2\pi)^3 \varepsilon_0} \int \frac{A_{nm}^z A_{mn}^z}{\hbar\omega + \varepsilon_{nm}} \rho_{mm}^{(0)}(\vec{k}) d\vec{k} - \frac{e^2}{(2\pi)^3 \varepsilon_0} \int \frac{A_{nm}^z A_{mn}^z}{\hbar\omega - \varepsilon_{nm}} \rho_{nn}^{(0)}(\vec{k}) d\vec{k} \quad (\text{M14})$$

The quality of crystal sample is usually imperfect due to impurities or defects; the scattering relation is considered by replacing $\hbar\omega \rightarrow \hbar\omega - i\eta$. For example, the dielectric tensor ε_{zz} is modified as,

$$\varepsilon_{zz} = 1 + \frac{e^2}{(2\pi)^3 \varepsilon_0} \int \frac{A_{nm}^z A_{mn}^z}{\hbar\omega + \varepsilon_{nm} - i\eta} \rho_{mm}^{(0)}(\vec{k}) d\vec{k} - \frac{e^2}{(2\pi)^3 \varepsilon_0} \int \frac{A_{nm}^z A_{mn}^z}{\hbar\omega - \varepsilon_{nm} - i\eta} \rho_{nn}^{(0)}(\vec{k}) d\vec{k}. \quad (\text{M15})$$

The complex refractive index N is defined as $N^2 = (n + ik)^2 = n^2 - k^2 + 2ink = \varepsilon_1 + i\varepsilon_2$, where n and k are the refractivity and attenuation coefficient, respectively, and $\varepsilon_1(\varepsilon_2)$ is the real (imaginary) part of the dielectric tensor. The real refractive index $n_{il}(\omega) = \sqrt{\frac{|\varepsilon| + \varepsilon_1}{2}}$, and

$$n_{zz}(\omega) = 1 + \frac{\alpha\gamma_z}{\hbar\omega + E_g} - \frac{\alpha\gamma_z}{\hbar\omega - E_g} \quad (\text{M16})$$

$$n_{xx}(\omega) = 1 + \frac{\alpha\gamma_x}{\hbar\omega + E_g} - \frac{\alpha\gamma_x}{\hbar\omega - E_g} \quad (\text{M17})$$

in case of far from resonance, that is, $\hbar\omega \ll E_g$. We put all constant into α , which can be further absorbed into γ_i , and the refractivity index at low frequency reads

$$n_{ii}(\omega) - 1 = \frac{\gamma_i}{\hbar\omega + E_g} - \frac{\gamma_i}{\hbar\omega - E_g} \propto \frac{\gamma_i}{E_g}, \quad (\text{M18})$$

in which γ_i characterizes the anisotropic strength of bonding in dimension of energy.

Data availability

The data that support the findings of this study are available from the corresponding author on reasonable requests.

Acknowledgements

This work was financially supported by the National Key R&D Program of China (2021YFA0717800), National Natural Science Foundation of China (52002397, U2003131), West Light Foundation of CAS (XBZG-ZDSYS-202201, 2020-XBQNXZ-002), Young Elite Scientist Sponsorship Program by CAST (YESS20200068), Natural Science Foundation of Xinjiang (2022D01E087), Key Research and Development Program of Xinjiang (2022B01023-3), Key Research Program of Frontier Sciences, CAS (ZDBS-LY-SLH035), High-level Talent Project of Xinjiang Uygur Autonomous Region (2020000039), Xinjiang Tianshan Talent Program (2022TSYCCX0071), and CAS Project for Young Scientists in Basic Research (YSBR-024). We thank Z. Xu, S. Zhang and F. Zhang at Technical Institute of Physics and

Chemistry, Chinese Academy of Sciences for their help with the tunable 193.2–200 nm light generation measurements; G. Zhang and B. Li at Fujian Institute of Research on the Structure of Matter, Chinese Academy of Sciences for their help with 266 nm light generation and NLO coefficients test.

Author contributions

M. Mutailipu proposed the idea and performed the data analysis and paper writing. J. Han grew the single crystals. Z. Li developed the theoretical calculations. F. Li and Z. Yang performed data analysis of theoretical results. J. Li and F. Zhang assisted with the optical performance characterization. X. Long supervised the crystal growth and the laser output experiments. S. Pan conceived the idea and supervised the project. All of the authors discussed the results and commented on the manuscript.

Competing interests

The authors declare no competing interests.

Additional information

Supplementary information The online version contains supplementary material available at <https://doi.org/10.1038/s41566-023-01228-7>.

Correspondence and requests for materials should be addressed to Shilie Pan.

Peer review information *Nature Photonics* thanks Gerard Aka and the other, anonymous, reviewer(s) for their contribution to the peer review of this work.

Reprints and permissions information is available at www.nature.com/reprints.